



HAL
open science

Synthesis, crystal structure and ^{19}F NMR parameters modelling of Catif_6(H_2o)_2 yielding to a revision of the bond-valence parameters for the $\text{Ti}^{4+}/\text{F}^{-}$ ion pair

Christophe Legein, Monique Body, Jérôme Lhoste, Wei Li, Thibault Charpentier, Damien Dambournet

► To cite this version:

Christophe Legein, Monique Body, Jérôme Lhoste, Wei Li, Thibault Charpentier, et al.. Synthesis, crystal structure and ^{19}F NMR parameters modelling of Catif_6(H_2o)_2 yielding to a revision of the bond-valence parameters for the $\text{Ti}^{4+}/\text{F}^{-}$ ion pair. Journal of Solid State Chemistry, 2023, 319, pp.123793. 10.1016/j.jssc.2022.123793 . cea-03830435v2

HAL Id: cea-03830435

<https://cea.hal.science/cea-03830435v2>

Submitted on 19 Oct 2023

HAL is a multi-disciplinary open access archive for the deposit and dissemination of scientific research documents, whether they are published or not. The documents may come from teaching and research institutions in France or abroad, or from public or private research centers.

L'archive ouverte pluridisciplinaire **HAL**, est destinée au dépôt et à la diffusion de documents scientifiques de niveau recherche, publiés ou non, émanant des établissements d'enseignement et de recherche français ou étrangers, des laboratoires publics ou privés.



HAL
open science

Synthesis, Crystal Structure and ^{19}F Nmr Parameters Modelling of $\text{Catif6}(\text{H}_2\text{O})_2$ Yielding to a Revision of the Bond-Valence Parameters for the $\text{Ti}^{4+}/\text{F}^-$ Ion Pair

Christophe Legein, Monique Body, Jérôme Lhoste, Wei Li, Thibault Charpentier, Damien Dambournet

► To cite this version:

Christophe Legein, Monique Body, Jérôme Lhoste, Wei Li, Thibault Charpentier, et al.. Synthesis, Crystal Structure and ^{19}F Nmr Parameters Modelling of $\text{Catif6}(\text{H}_2\text{O})_2$ Yielding to a Revision of the Bond-Valence Parameters for the $\text{Ti}^{4+}/\text{F}^-$ Ion Pair. SSRN Electronic Journal, 2022, 10.2139/ssrn.4253528 . cea-03830435

HAL Id: cea-03830435

<https://hal-cea.archives-ouvertes.fr/cea-03830435>

Submitted on 26 Oct 2022

HAL is a multi-disciplinary open access archive for the deposit and dissemination of scientific research documents, whether they are published or not. The documents may come from teaching and research institutions in France or abroad, or from public or private research centers.

L'archive ouverte pluridisciplinaire **HAL**, est destinée au dépôt et à la diffusion de documents scientifiques de niveau recherche, publiés ou non, émanant des établissements d'enseignement et de recherche français ou étrangers, des laboratoires publics ou privés.

Synthesis, crystal structure and ^{19}F NMR parameters modelling of $\text{CaTiF}_6(\text{H}_2\text{O})_2$ yielding to a revision of the bond-valence parameters for the $\text{Ti}^{4+}/\text{F}^-$ ion pair

Christophe Legein^{a,*}, Monique Body^a, Jérôme Lhoste^a, Wei Li^{b,c}, Thibault Charpentier^d, Damien Dambournet^{b,c}

^a Institut des Molécules et Matériaux du Mans (IMMM) - UMR 6283 CNRS, Le Mans Université, Avenue Olivier Messiaen, 72085 Le Mans Cedex 9, France

^b Sorbonne Université, CNRS, Physicochimie des Electrolytes et Nanosystèmes Interfaciaux, PHENIX, F-75005 Paris, France

^c Réseau sur le Stockage Electrochimique de l'Energie (RS2E), FR CNRS 3459, 80039 Amiens Cedex, France

^d Université Paris-Saclay, CEA, CNRS, NIMBE, 91191 Gif-sur-Yvette cedex, France

e-mail address of each author:

christophe.legein@univ-lemans.fr; monique.body@univ-lemans.fr;

Jerome.Lhoste@univ-lemans.fr; liwei1218@gmail.com ; thibault.charpentier@cea.fr;

damien.dambournet@sorbonne-universite.fr

Corresponding Author:

christophe.legein@univ-lemans.fr (Christophe Legein),

Abstract

$\text{CaTiF}_6(\text{H}_2\text{O})_2$ was synthesized by a solvothermal method and was found to be isostructural to $\text{SrTiF}_6 \cdot 2\text{H}_2\text{O}$. The structure, refined from Powder X-Ray Diffraction (PXRD) data, is built from the connectivity of dimers $[\text{Ca}_2\text{F}_{10}(\text{H}_2\text{O})_4]$ of square antiprisms (SAP) $[\text{CaF}_5(\text{H}_2\text{O})_3]$ and TiF_6 octahedra. To assign the six ^{19}F resonances to the six fluorine crystallographic sites of same multiplicity, ^{19}F magnetic shielding tensors have been calculated using the GIPAW method. Unusually, the plot of the experimental ^{19}F isotropic chemical shift (δ_{iso}) values, as a function of the calculated ^{19}F isotropic shielding (σ_{iso}) values, shows a much better alignment for the experimental than for the DFT-optimized structure. Whereas, the dynamics of the structural water molecules under experimental conditions are not captured by the optimized structure, the experimental averaged structure provides a good account of the experimental data and a reliable assignment of the ^{19}F resonances to the F sites. Finally, the previously established bond-valence (BV) parameter R_{ij} for the $\text{Ti}^{4+}/\text{F}^-$ ion pair (1.76 Å) leads to overestimated BV sum values for Ti. This trend has been observed for almost all other fluorotitanates. We then undertook to refine its value, using the Ti-F bond lengths from 70 carefully selected structures containing 134 Ti sites forming TiF_6 octahedra, and leading to $R_{ij} = 1.706$ Å.

Keywords

Inorganic hydrated hexafluorotitanate (or Inorganic fluorides); Powder X-ray diffraction; Crystal structure; ^{19}F solid state NMR; DFT calculations, Bond-valence

1. Introduction

The solid state chemistry of titanium(IV) fluoride complex presents a rich structural diversity. Numerous anionic (in which the titanium atom is present as a complex anion) fluoride complexes of Ti(IV) with various inorganic and organic cations have been synthesized and structurally studied [1]. Some of them possess properties of interest such as gas adsorption ($[\text{Cu}(\text{bipy})_2\text{TiF}_6]$, [2]), negative thermal expansion (CaTiF_6 , [3]), photoluminescence when doped by Mn^{4+} (K_2TiF_6 [4] and Cs_2TiF_6 [5]) and $[\text{Cu}(\text{bpy})_2(\text{H}_2\text{O})]_2[\text{TiF}_6]_2 \cdot 3\text{H}_2\text{O}$ is noncentrosymmetric [6]. $\text{CaTiF}_6(\text{H}_2\text{O})_2$ does not have interesting properties or these have not yet been identified. Nevertheless, its synthesis and its structure determination were not useless as the reader will see.

$\text{CaTiF}_6(\text{H}_2\text{O})_2$ expands the list of inorganic hydrated hexafluorotitanates which includes, in addition to $\text{SrTiF}_6(\text{H}_2\text{O})_2$ [7,8], of which $\text{CaTiF}_6(\text{H}_2\text{O})_2$ is isotype, $\text{M}(\text{H}_2\text{O})_6(\text{TiF}_6)$ with $\text{M} = \text{Mn}, \text{Zn}$ [9,10] and Ni [11], $\text{Cu}(\text{H}_2\text{O})_4\text{TiF}_6$ [12], $\text{Li}_2\text{TiF}_6(\text{H}_2\text{O})_2$ [13], $(\text{NH}_3\text{OH})_2(\text{TiF}_6)(\text{H}_2\text{O})_2$ [14] and $(\text{H}_5\text{O}_2)_2(\text{TiF}_6)(\text{H}_2\text{O})_2$ [15]. $\text{NH}_4\text{CuTiF}_7(\text{H}_2\text{O})_4$ [16] does not meet the definition of hexafluorotitanate but also presents isolated $[\text{TiF}_6]^{2-}$ octahedral complexanions.

After its synthesis, the refinement of the structure of $\text{CaTiF}_6(\text{H}_2\text{O})_2$ from powder X-ray diffraction (PXRD) data is reported. While the Ti-F bond lengths in $\text{CaTiF}_6(\text{H}_2\text{O})_2$ are not unusual, due to poorly determined bond-valence (BV) parameters for the $\text{Ti}^{4+}/\text{F}^-$ ion pair, the BV sum (BVS) of Ti significantly differs from its atomic valence (oxidation state). We therefore decided to refine the BV parameters for the $\text{Ti}^{4+}/\text{F}^-$ ion pair.

Then, the ^{19}F solid state NMR spectrum of $\text{CaTiF}_6(\text{H}_2\text{O})_2$ is reported to confirm the number of inequivalent fluorine crystallographic sites and their relative multiplicities and DFT calculations of the ^{19}F magnetic shielding tensors have been performed, using the Gauge Including Projector Augmented Waves (GIPAW) method [17,18], to assign the ^{19}F NMR resonances to the crystallographic sites. In the present case, the dynamics of the

structural water molecules under experimental conditions are not captured by the DFT geometry optimized structure at 0 K leading to a poorer quality of the calculations after geometry optimization.

2. Materials and methods

2.1. Material preparation

$\text{CaTiF}_6(\text{H}_2\text{O})_2$ was synthesized by a solvothermal synthesis. 750 mg (6.75 mmol) of CaCl_2 were dissolved into isopropanol inside a Teflon liner cup. 2 mL (6.75 mmol) of titanium isopropoxide and a variable volume of HF (aqueous hydrofluoric acid - 40 %), depending on the desired molar ratio $\text{F}/(\text{Ca}+\text{Ti})$ ratio, were respectively added in the solution under stirring. *Caution: HF is toxic and corrosive and should be handled with appropriate protective equipment and training.* The volume of isopropanol used for the dissolution of CaCl_2 was calculated based on a total solution volume of 30 mL. Teflon liner cup was placed inside a stainless-steel autoclave and then heated in an oven at 90 °C for 12 h. After that, the autoclave was left to cool down to room temperature. The resulting white precipitate was washed twice with ethanol and subsequently recovered by centrifugation at 4400 rpm for 15 min. Finally, the powder was dried at 80 °C for 2 h.

2.2. Characterization methods

2.2.1. Powder X-ray diffraction and structural analysis

PXRD data were collected at room temperature using a Rigaku diffractometer, equipped with $\text{Cu K}\alpha$ radiation, in a Bragg-Brentano geometry. For the structural determination, PXRD analyses were performed with a PANalytical X'Pert Pro diffractometer with $\text{Cu K}\alpha$ radiation. A high resolution diffractogram was recorded at room temperature in the $[5-130]^\circ 2\theta$ range with a 0.013° step (scan time of ~ 2 h). The Rietveld method [19] implemented in the Fullprof program [20] was used for the structural refinement. Background level was made manually. Atomic positions, as well as

isotropic displacement parameters, were refined. Crystal structure of $\text{CaTiF}_6(\text{H}_2\text{O})_2$ has been deposited via the joint CCDC/FIZ Karlsruhe deposition service. CSD [21] 2163652 (deposition number) contains the supplementary crystallographic data for this paper. These data can be obtained free of charge from FIZ Karlsruhe via www.ccdc.cam.ac.uk/structures.

2.2.2. Thermogravimetric analyses

The thermogravimetric analyses (TGA) were performed using Setaram Setsys equipment. The sample was heated from room temperature up to 600 °C under helium atmosphere (heating rate = 5 °C/min).

2.2.3. Solid state NMR

^1H and ^{19}F solid-state Magic Angle Spinning (MAS) NMR experiments were performed on a Bruker Avance III spectrometer operating at 7.0 T (^1H and ^{19}F Larmor frequencies of 300.1 and 282.4 MHz, respectively), using a 1.3 mm CP-MAS probe head. The ^1H and ^{19}F MAS spectra were recorded using a Hahn echo sequence with an interpulse delay equal to one rotor period. For ^{19}F , the 90° pulse length was set to 1.55 μs and the recycle delay was set to 20 s. For ^1H , the 90° pulse length was set to 1.13 μs and the recycle delay was set to 120 s. ^1H and ^{19}F spectra are referenced to TMS and CFCl_3 , respectively, and they were fitted by using the DMFit software [22].

To quantify the proton content on the sample, ^1H solid-state MAS NMR spectra were also recorded for an organic crystalline solid, adamantane (Tricyclo-[3.3.1.1^{3,7}]decane, $((\text{CH})_4(\text{CH}_2)_6)$, and the mass of each sample in the rotor was measured. The fits of the Hahn echo spectra allow one to determine the integrated intensities for each sample. Because, for each sample, the recycle delays were chosen to ensure that the amount of signal detected is maximum (20 s for adamantane), we assume that the integrated

intensities are proportional to the number of scans and the molar quantity of H atoms in the rotor [23].

2.3 Bond-valence calculations

Individual BV values were calculated using [6,7] $v_{ij} = \exp [(R_{ij} - d_{ij})/b]$ where v_{ij} is the valence of the bond ij , d_{ij} is the length of the bond ij and R_{ij} , the notional length of a bond of unit valence, and b , the softness parameter, are empirical constants dependent on the bonded elements i and j : $R_{ij} = 1.76 \text{ \AA}$ [25] and the value we have refined, $R_{ij} = 1.706 \text{ \AA}$, 1.87 \AA [26], 1.967 \AA [24] and $b = 0.37 \text{ \AA}$ for Ti-F, Ca-F, Ca-O, respectively, $R_{ij} = 0.708 \text{ \AA}$ and $b = 0.558 \text{ \AA}$ for H-F [27], $R_{ij} = 0.907 \text{ \AA}$ and $b = 0.28 \text{ \AA}$ for H-O $< 1.05 \text{ \AA}$ and $R_{ij} = 0.99 \text{ \AA}$ and $b = 0.59 \text{ \AA}$ for H-O $> 1.70 \text{ \AA}$ [28]. The valence, v_{ij} , of a bond between two atoms i and j is defined such that the sum of all the bond-valences (BVS) for a given atom i with valence V_i obeys: $\sum_j v_{ij} = V_i$.

2.4 DFT calculations

^1H and ^{19}F magnetic shielding tensor calculations were performed using the GIPAW approach [17,18] as implemented in the CASTEP code [29,30]. The Perdew–Burke–Ernzerhof (PBE) functional [31] was employed in the generalized gradient approximation (GGA) for the exchange correlation energy and ultrasoft pseudopotentials (USPP) were used to describe core-valence interactions [18]. The wave functions were expanded on a plane-wave basis set with a kinetic energy cutoff of 700 eV. The total energy was converged up to change below 1×10^{-8} eV. The Brillouin zone was sampled using a Monkhorst-Pack grid spacing of 0.04 \AA^{-1} (corresponding to a k-point mesh of $5 \times 3 \times 3$). NMR parameters were calculated using “on-the-fly” USPP provided in CASTEP. Core radii of 0.8, 1.3, 1.4, 1.6 and 1.8 a. u. were used for H, O, F, Ca and Ti respectively, with 1s valence orbitals for H, 2s and 2p valence orbitals for O and F, and 3s, 3p, 4s and 3d valence orbitals for Ca and Ti. The default definition of the Ca USPP proposed by the Materials Studio

package was modified by shifting to higher energy (1.81 eV) the local potentials of the Ca²⁺ ion (3d⁰) USPP in order to overcome the deficiency of the PBE functional which generates, in the present case, too much covalency between the Ca 3d empty states and the anionic fluoride 2p levels [32,33].

Computations of the NMR parameters were performed for experimental (EXP) and atomic positions geometry optimized (APO) structures. APO structures were obtained by minimizing the residual forces ($|F|_{\max}$ below 10 meV.Å⁻¹) for all atoms, using the Broyden-Fletcher-Goldfarb-Shanno (BFGS) method and keeping symmetry constraints and fixing cell parameters to experimentally measured values [34].

To enhance the robustness of the approach, atomic position optimizations as well as GIPAW calculations of the magnetic shielding tensors were also performed with the Vienna Ab Initio Simulation Package (VASP) (5.3) [35,36]. The GGA PBE functional [31] was also employed, using the PAW potentials [37,38] from the VASP library (Ca_sv_GW, Ti_sv_GW, F_GW, O_GW and H_GW) for the description of the core electrons. The DFT-D3 method corrections of Grimme et al. [39] which are expected to be more efficient for the non-covalent interactions, were included since in CaTiF₆(H₂O)₂ the protons of the water molecules can potentially form H-bonds with the F⁻ ions at the vertices of the TiF₆²⁻ octahedra and/or with another water molecule. Structures were first optimized (APO and fully optimized (FO)) with a plane wave cutoff of 550 eV (forces minimized below 5 meV/Å) and a 3x2x2 Monkhorst-Pack grid of k-points. GIPAW-NMR calculations of the magnetic shielding tensors were performed using the same parameters.

The chemical shift (magnetic shielding) tensor is described by three parameters, the isotropic chemical shift (shielding), δ_{iso} (σ_{iso}), the chemical shift (shielding) anisotropy, δ_{csa} (σ_{csa}), and the asymmetry parameter, η_{csa} , defined as: $\delta_{\text{iso}} = (\delta_{\text{xx}} + \delta_{\text{yy}} + \delta_{\text{zz}})/3$ ($\sigma_{\text{iso}} = (\sigma_{\text{xx}} + \sigma_{\text{yy}} + \sigma_{\text{zz}})/3$), $\delta_{\text{csa}} = \delta_{\text{zz}} - \delta_{\text{iso}}$ ($\sigma_{\text{csa}} = \sigma_{\text{zz}} - \sigma_{\text{iso}}$) and $\eta_{\text{csa}} = (\delta_{\text{yy}} - \delta_{\text{xx}})/\delta_{\text{csa}}$ ($\eta_{\text{csa}} = (\sigma_{\text{yy}} - \sigma_{\text{xx}})/$

σ_{csa}). δ_{ii} (σ_{ii}) are the principal components of the chemical shift (shielding) tensor defined in the sequence $|\delta_{zz} - \delta_{\text{iso}}| \geq |\delta_{xx} - \delta_{\text{iso}}| \geq |\delta_{yy} - \delta_{\text{iso}}|$ ($|\sigma_{zz} - \sigma_{\text{iso}}| \geq |\sigma_{xx} - \sigma_{\text{iso}}| \geq |\sigma_{yy} - \sigma_{\text{iso}}|$). The isotropic chemical shift is defined as $\delta_{\text{iso}} \approx -\sigma_{\text{iso}} + \sigma_{\text{ref}}$. The ^1H δ_{iso} values have been calculated by using this equation with $\sigma_{\text{ref}} = 31.0$ ppm [40]. The ^{19}F δ_{iso} values have been calculated by using the equations ($\delta_{\text{iso}} = -a\sigma_{\text{iso}} + \sigma_{\text{ref}}$) of the linear regressions between the calculated σ_{iso} values and the experimental δ_{iso} values for the studied compound.

3. Results and Discussion

3.1. Synthesis and phase composition

$\text{CaTiF}_6(\text{H}_2\text{O})_2$ was synthesized by a solvothermal route. The amount of fluoride, defined thereafter as the molar ratio $R = \text{F}/(\text{Ca}+\text{Ti})$, was investigated as a reaction parameter. It was varied from 1 to 3 with equimolar quantities of Ca and Ti. The PXRD patterns of the samples obtained for different R values (**Fig. 1**) show that the nature of the stabilized compounds is greatly influenced by the added fluorine content. For $R=1$, the PXRD pattern shows Bragg peaks characteristic of CaF_2 (fluorite, $Fm\bar{3}m$ [41]) and TiO_2 (anatase, $I4_1/amd$ [42]). Using a similar chemical system, we previously showed that a pure oxide TiO_2 cannot be formed and instead a complex composition such as $\text{Ti}_{1-x-y}\square_{x+y}\text{O}_{2-4(x+y)}\text{F}_{4x}(\text{OH})_{4y}$ (\square : titanium vacancy) was obtained, suggesting the possible stabilization of fluoride within the vicinity of Ti^{4+} [43]. Increasing the fluorine content to $R = 2$ yields to the destabilization of these phases and, even if well defined, the pattern could not be indexed. Further increasing the fluorine content yields to the appearance of a new phase with a well-crystallized compound obtained at $R = 3$ which corresponds to the composition of CaTiF_6 . The PXRD pattern, however, is not consistent with this compound which crystallizes in a rhombohedrally-distorted ReO_3 structure [44]. An ICSD [45] web database search in the M-Ti-F-O-H (M : alkaline earth) system enables the identification of one compound with similar X-ray features, $\text{SrTiF}_6(\text{H}_2\text{O})_2$ (ICSD 20655 [7])

and ICSD 200511 and 200512 [8]) suggesting that the sample prepared at $R = 3$ consists of $\text{CaTiF}_6(\text{H}_2\text{O})_2$ and adopts the same crystal structure that $\text{SrTiF}_6(\text{H}_2\text{O})_2$. This assumption was supported by the ^{19}F solid-state MAS NMR spectrum of $\text{CaTiF}_6(\text{H}_2\text{O})_2$ showing six resonances of similar intensities (see below) since the crystal structure of $\text{SrTiF}_6(\text{H}_2\text{O})_2$ contains six F sites of the same multiplicity.

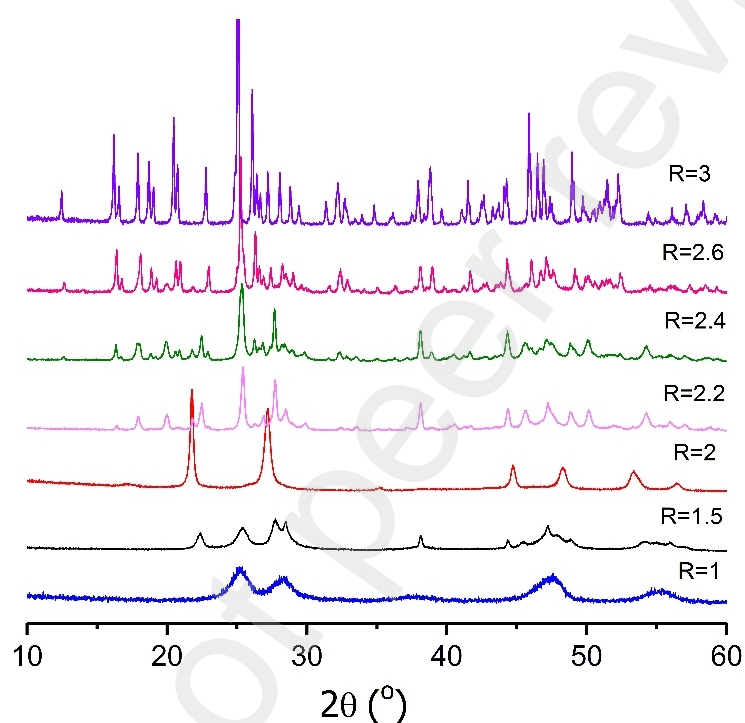


Fig. 1. PXRD patterns of the samples prepared using different molar ratio $R = \text{F}/(\text{Ca}+\text{Ti})$.

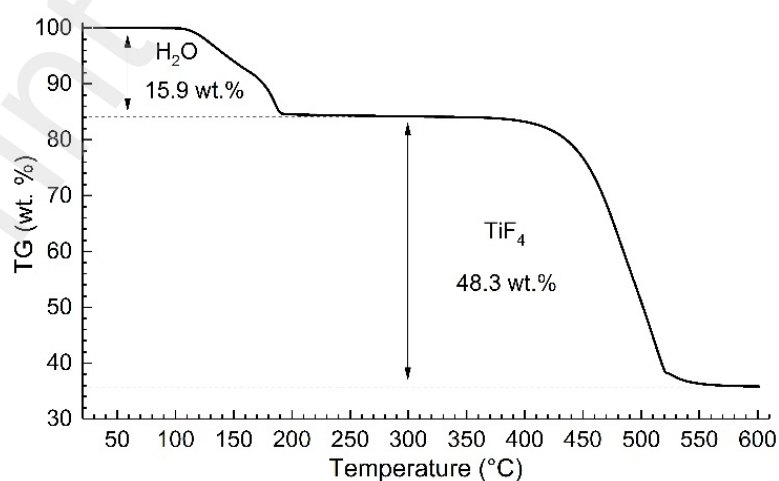


Fig. 2. Thermogravimetric curve for the sample obtained at $R = 3$.

The phase composition $\text{CaTiF}_6(\text{H}_2\text{O})_2$ was confirmed by TGA, supported by proton quantification using ^1H solid-state MAS NMR. The TG curve (**Fig. 2**) shows two weight loss steps. The first weight loss occurs at 100-200 °C and is assigned to the departure of water molecules. The expected weight loss corresponding to the dehydration of $\text{CaTiF}_6(\text{H}_2\text{O})_2$ is 15.1 wt% which is close to those obtained experimentally, *i.e.*, 15.9 wt%. The difference might be due to pyrohydrolysis reaction induced by the released water molecule according to: $\text{Ti-F} + \text{H}_2\text{O} \rightarrow \text{Ti-OH} + \text{HF}$ [46]. The experimental value of ^1H wt %, 1.65 (0.10) %, is indeed close to the expected value, 1.69 %. The second weight loss appears at $T > 400$ °C and is assigned to the departure of gaseous TiF_4 [47] leading to the formation of CaF_2 . The experimental weight loss of 48.3 wt% is lower than expected (52.0 wt%) which can mainly be explained by a partial hydrolysis occurring during the first step. The amount of CaF_2 present as an impurity (see 3.4) is indeed too low (1% of the F atoms) to explain this difference alone.

3.2. Crystal structure

Rietveld analysis of the PXRD pattern was performed to determine the crystal structure of $\text{CaTiF}_6(\text{H}_2\text{O})_2$ starting from the crystal structure of $\text{SrTiF}_6(\text{H}_2\text{O})_2$ determined on single crystal at 173 K (ICSD 200512, [8]) for which the H atomic positions have been determined. Nevertheless, the positions of the H atoms vary significantly when refining the structure from a PXRD diagram. Moreover, H atoms are difficult to locate accurately using XRD data since the obtained covalent bond lengths involving H atoms are appreciably shorter than those obtained from neutron diffraction data or after DFT optimizations, which both provide reliable H positions [34]. The atomic positions of the first obtained structural model were then DFT optimized using CASTEP and further refined with restrained O-H bond length ($0.990 (\pm 0.001)$ Å) and H-H intramolecular distance ($1.580 \text{ \AA} (\pm 0.001) \text{ \AA}$, corresponding to a H-O-H angle value equal to 106°), in the

H₂O molecules. This bond length and this distance are in close agreement with the experimental values inferred from neutron diffraction data [49]. The Rietveld refinement is presented **Fig. 3**. Crystal data and the result of the refinement are reported in **Table 1**, the atomic positions are collected in **Table S1** and bond lengths and interatomic distances are summarized in **Table S2**.

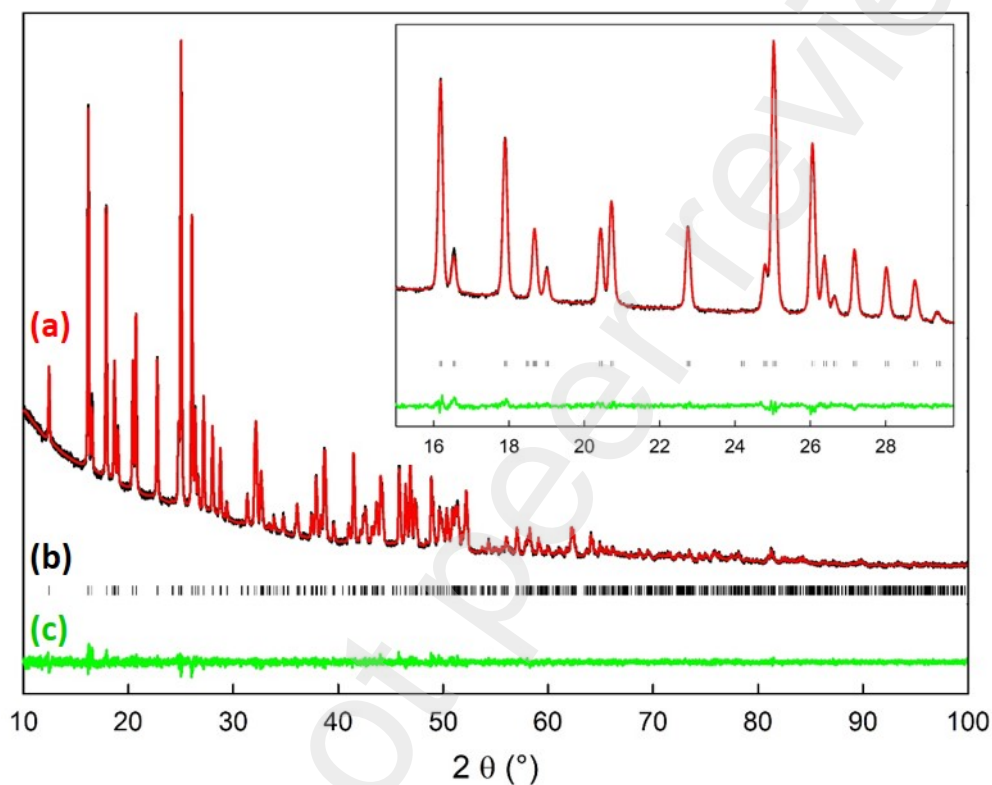


Fig. 3. Rietveld refinement (*P2/n* SG) of the PXRD pattern of CaTiF₆(H₂O)₂; (a) experimental (in black) and calculated (in red) patterns; (b) Bragg positions; (c) difference between experimental and calculated patterns. The inset shows a zoom of a selected 2θ range.

Table 1. Crystal data and result of the refinement of $\text{CaTiF}_6(\text{H}_2\text{O})_2$.

| | |
|--|-------------|
| Molecular weight (g.mol^{-1}) | 475.92 |
| Crystal system | monoclinic |
| SG | $P2_1/n$ |
| a (Å) | 5.8798(2) |
| b (Å) | 10.8546(4) |
| c (Å) | 9.5096(3) |
| γ (°) | 98.9869(9) |
| V (Å ³) | 599.48(3) |
| Z | 2 |
| $\rho_{\text{calc.}}$ (g.cm^{-3}) | 2.6366 |
| Wavelength (Å) | 1.54056 |
| 2θ range (°) | 5-130 |
| Refl. unique | 2118 |
| Refined parameters | 57 |
| R_p/R_{wp} | 0.113/0.098 |
| R_B/R_F | 0.030/0.038 |

The structure is built from the connectivity by edges of distorted square antiprism (SAP) $[\text{CaF}_5(\text{H}_2\text{O})_3]$ and by corners of distorted SAP with TiF_6 octahedra (**Fig. 4**). The Ca-F bond lengths are in common range of 2.326-2.436 Å (Ca-F = 2.367 Å in CaF_2 [25]). The TiF_6 octahedron is slightly distorted with Ti-F bond lengths in the range 1.797-1.876 Å (**Table S1**) and angular distortions all below 4° (**Table S3**). The BVS V_i for all atoms in $\text{CaTiF}_6(\text{H}_2\text{O})_2$ are gathered in **Table 2**. The average bond length (1.833 Å) is shorter than those found in $\text{SrTiF}_6(\text{H}_2\text{O})_2$ (1.860 Å). Nevertheless, these somewhat short Ti-F bond lengths do not explain, or not alone, the high values of BVS for Ti (4.94) and F (ranging from 1.10 to 1.15). In fact, as we will show later, the value of the parameter R_{ij} of the $\text{Ti}^{4+}/\text{F}^-$ ion pair is erroneous.

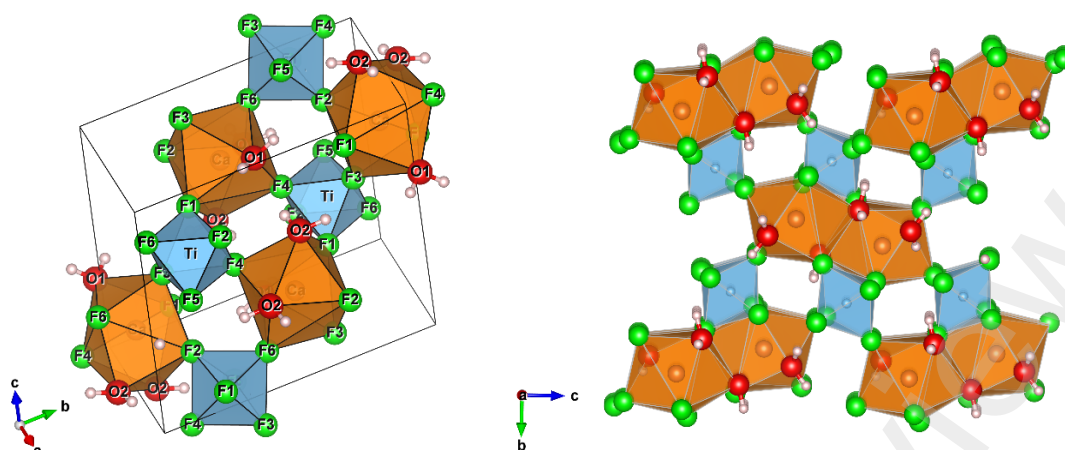


Fig. 4. Representations (left :perspective view; right: projection in (\vec{b}, \vec{c}) plane) of the crystal structure of $\text{CaTiF}_6(\text{H}_2\text{O})_2$. The atoms of Ca, Ti, O, F and H are represented in orange, blue, red, green and white, respectively.

Table 2. Atoms i and j , length of the bond ij , d_{ij} (\AA), for $i = \text{Ti, Ca}$ and H, and BVS V_i for all atoms in $\text{CaTiF}_6(\text{H}_2\text{O})_2$. In italic and between parentheses, V_i values for $i = \text{Ti}$ and F calculated with the revised value of R_{ij} .

| i | j | d_{ij} | V_i | j | j | d_{ij} | V_i | i | V_i |
|-----------|----------|----------------------------|-------------------------|-----------|----------|----------------------------|-------------------------|-----------|-------------------------|
| Ti | F3 | 1.797 | 4.94 (4.27) | H1 | O1 | 0.990 | 0.82 | F1 | 1.13 (1.02) |
| | F5 | 1.803 | | | F5 | 2.495 | | F2 | 1.10 (1.00) |
| | F6 | 1.830 | | | F1 | 2.567 | | F3 | 1.12 (1.00) |
| | F1 | 1.837 | | H2 | O1 | 0.991 | 0.90 | F4 | 1.13 (1.03) |
| | F2 | 1.854 | | | F5 | 1.896 | | F5 | 1.15 (1.03) |
| | F4 | 1.876 | | | F2 | 2.554 | | F6 | 1.14 (1.03) |
| Ca | F2 | 2.326 | 2.04 | H3 | O2 | 0.990 | 0.96 | O1 | 1.87 |
| | F6 | 2.331 | | | F4 | 2.170 | | O2 | 1.88 |
| | F4 | 2.336 | | | O1 | 2.334 | | | |
| | F1 | 2.341 | | | F4 | 2.539 | | | |
| | O1 | 2.436 | | H4 | O2 | 0.990 | 0.87 | | |
| | F3 | 2.436 | | | F5 | 2.006 | | | |
| | O2 | 2.568 | | | F6 | 2.691 | | | |
| | O2 | 2.568 | | | | | | | |

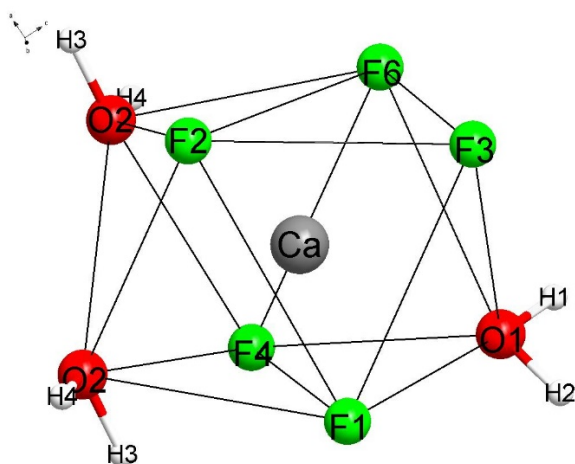


Fig. 5. Perspective view of the $[\text{CaF}_5(\text{H}_2\text{O})_3]$ SAP. Atoms are labelled.

For a SAP based on equal edge lengths (hard sphere model) and all metal–ligand bond lengths equal to d_0 , the angle that the eight metal–ligand bonds make with the fourfold axis, is equal to 59.3° , the angle between metal–ligand bonds for adjacent ligands is equal to 74.9° , the angle between metal–ligand bonds for opposite ligands, is equal to 141.6° , and the edge length is $1.216 d_0$ [50]. In the $[\text{CaF}_5(\text{H}_2\text{O})_3]$ SAP (**Fig. 5**), the average angle between metal–ligand bonds for adjacent ligands is equal to 76.0° , the angle between metal–ligand bonds for opposite ligands, is equal to 141.1° (**Table S4**), the average metal–ligand bond lengths is equal to 2.420 \AA (**Table S2**) and the average edge length is equal to 2.974 \AA (**Table S5**), leading to a ratio average edge length on average metal–ligand bond length equal to 1.229. The extended view of the unit cell (**Fig. 4b**) shows that $[\text{CaF}_5(\text{H}_2\text{O})_3]$ SAP are connected one another forming dimers via edge-sharing of two water molecules ($\text{Ca-O2} = 2.568 \text{ \AA}$, $\text{O2-O2} = 2.952 \text{ \AA}$). The third water molecule within $[\text{CaF}_5(\text{H}_2\text{O})_3]$ SAP forms a terminal Ca-O1 bond (2.436 \AA), which is H-bonded by H2 with one of the terminal F atom (F5) of TiF_6 octahedra: $\text{H2-F5} = 1.896 \text{ \AA}$, $\text{O1-F5} = 2.753 \text{ \AA}$ and $\text{O1-H2-F5} = 142.9^\circ$. Indeed, there is in $\text{CaTiF}_6(\text{H}_2\text{O})_2$ a fairly dense H-bonding network (**Fig. 6**) considering the number of potential donors (6 F and 2 O atoms) and acceptors (4 H atoms). There are in fact seven $\text{O-H}\cdots\text{Y}$ ($\text{Y} = \text{F}, \text{O}$) contacts with angle larger than 120°

and H...Y distances smaller than the sum of H (1.20 Å) and Y (O: 1.52 Å; F: 1.47 Å) van der Waals radii [51] (**Table 3**). While among the Y atoms, F5 is the only one engaged in three contacts satisfying these criteria, except H4, each H atom is engaged in two contacts satisfying these criteria and therefore likely to form H-bonds with two different Y atoms in the course of time, keeping in mind the rotational movement of water molecules enabling formation and breaking of these H-bonds. Among these seven contacts, O1-H2...F5 is likely to give the strongest H-bond, since “the closer the angle is to 180°, the stronger the H-bond and the shorter the H...Y distance” [52]. Hence, the structure of $\text{CaTiF}_6(\text{H}_2\text{O})_2$ is built of dimers $[\text{Ca}_2\text{F}_{10}(\text{H}_2\text{O})_4]$ of $[\text{CaF}_5(\text{H}_2\text{O})_3]$ SAP. Each SAP is connected to five different TiF_6 octahedra by F1-4 and F6 atoms (**Fig. 4**). The only F atom which does not bridge TiF_6 octahedra and $[\text{CaF}_5(\text{H}_2\text{O})_3]$ SAP, F5, is strongly H bonded to a proton of the water molecule which not connects two SAP.

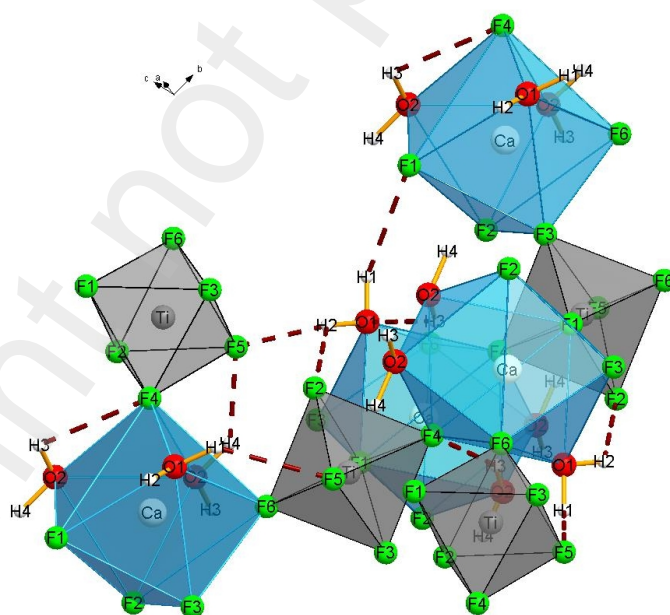


Fig. 6. Perspective view of the crystal structure of $\text{CaTiF}_6(\text{H}_2\text{O})_2$ on which the atoms are labeled and the H-bonds represented as brown dotted line.

Table 3. Geometries (\AA , $^\circ$) of the O–H \cdots Y (Y = F, O) contacts with angle larger than 120° and H \cdots Y distances smaller than the sum of H (1.20 \AA) and Y (O: 1.52 \AA ; F: 1.47 \AA) van der Waals radii in the EXP and in the APO (in *italic*) structures of $\text{CaTiF}_6(\text{H}_2\text{O})_2$.

| O–H \cdots Y | O–H | H \cdots Y | O \cdots Y | O–H \cdots Y |
|-------------------|---------------------|---------------------|---------------------|---------------------|
| O1–H2 \cdots F2 | 0.991 | 2.554 | 3.251 | 127.1 |
| O2–H3 \cdots F4 | 0.990 | 2.170 | 3.065 | 149.4 |
| O1–H1 \cdots F1 | 0.990/ <i>0.976</i> | 2.567/ <i>2.485</i> | 3.456/ <i>3.195</i> | 134.5/ <i>129.4</i> |
| O2–H3 \cdots O1 | 0.990/ <i>0.992</i> | 2.334/ <i>1.838</i> | 3.022/ <i>2.816</i> | 126.0/ <i>167.6</i> |
| O1–H1 \cdots F5 | 0.990/ <i>0.976</i> | 2.495/ <i>2.550</i> | 3.233/ <i>3.369</i> | 131.0/ <i>141.5</i> |
| O1–H2 \cdots F5 | 0.991/ <i>0.991</i> | 1.896/ <i>1.685</i> | 2.753/ <i>2.670</i> | 142.9/ <i>172.2</i> |
| O2–H4 \cdots F5 | 0.990/ <i>0.982</i> | 2.006/ <i>1.893</i> | 2.820/ <i>2.796</i> | 137.9/ <i>151.5</i> |

Table 4. Average, minimal (Min), maximal (Max) and standard deviation (σ) of the average Ti–F bond lengths, $\langle d_{\text{Ti-F}} \rangle$ (\AA) and of the BVS for Ti calculated using $R_{ij} = 1.760 \text{ \AA}$ [25] and (in *italic*) using the revised R_{ij} value, $R_{ij} = 1.706 \text{ \AA}$, of the 133 considered TiF_6 octahedron.

| | Average | Min | Max | σ |
|--------------------------------------|-------------|-------------|-------------|-------------|
| $\langle d_{\text{Ti-F}} \rangle$ | 1.865 | 1.790 | 1.907 | 0.013 |
| BVS ($R_{ij} = 1.760 \text{ \AA}$) | 4.62 | 4.05 | 5.07 | 0.12 |
| BVS ($R_{ij} = 1.706 \text{ \AA}$) | <i>4.00</i> | <i>3.50</i> | <i>4.38</i> | <i>0.10</i> |

3.3. Revised bond valence parameters for the $\text{Ti}^{4+}/\text{F}^-$ ion pair

A significant difference between the atomic valence (oxidation state) and BVS values for a given crystal structure (as observed in **Table 2** for $\text{CaTiF}_6(\text{H}_2\text{O})_2$) can be the result of either a poorly determined structural model or poorly determined BV parameters. Some BVS calculations on previously published crystal structures of fluorotitanates quickly showed that the BV parameters for the $\text{Ti}^{4+}/\text{F}^-$ ion pair almost systematically lead to overestimated BVS values for Ti.

In order to calculate the accurate BV parameters for the $\text{Ti}^{4+}/\text{F}^-$ ion pair, experimental Ti–F bond lengths were extracted from crystal structures deposited in the CSD [21] and

the ICSD [45]. 70 structures that fulfilled the following criteria were selected for calculations: (1) the oxidation number of Ti is equal to IV; (2) only F atoms are bounded to Ti; (3) structures are precisely determined ($R \leq 0.05$); (4) the occupancies of F and Ti atomic positions are equal to 1. Chemical formula, reference, ICSD code and/or CSD deposition number and/or CSD identifier, average Ti-F bond lengths (\AA) for each TiF_6 octahedron (Ti site), BVS for Ti calculated using $R_{ij} = 1.760 \text{ \AA}$ and $b = 0.37$ [25] are given as supplementary material in **Table S6**. The BVS values range from 4.05 to 5.07 and are in average equal to 4.63 (**Table 4**).

In these 70 structures, the 134 Ti sites are six fold coordinated by F atoms forming TiF_6 octahedra. For such ion pairs with a single coordination number, i.e., with a narrow range of individual BV values, v_{ij} , a refinement of both the R_{ij} and b parameters is not required. Indeed, the b parameter remains equal to its “universal” value of 0.37 \AA . Only the R_{ij} parameter has then been refined with the constraint that the average Ti BVS is equal to its oxidation state (atomic valence), i.e., 4.00. This condition is fulfilled for a value of R_{ij} equal to 1.706 \AA (**Table 4**).

The BVS calculated with this refined R_{ij} value for F (ranging from 1.00 to 1.03) and Ti (4.27) atoms in $\text{CaTiF}_6(\text{H}_2\text{O})_2$ are closer to the values of their oxidation states (**Table 2**).

3.4. ^{19}F and ^1H MAS NMR

The TiF_6 octahedron features six independent crystallographic F sites with an equivalent multiplicity (4e). Five F atoms are corner-shared with Ca polyhedra, while F5 is terminal and H-bonded with water molecules of the $\text{CaF}_5(\text{H}_2\text{O})_3$ SAP. The ^{19}F MAS NMR spectrum of $\text{CaTiF}_6(\text{H}_2\text{O})_2$, fitted with six NMR resonances (**Fig. 7**) of similar intensities (**Table 5**), supports the structural model (**Table S1**) and points to the distinction of the six crystallographic F sites. The NMR lines are symmetrical which shows the absence of hydroxylation of the F sites. Several weak lines not assigned to the compound reveal the

presence of a small amount of fluorinated impurities, including CaF_2 ($\delta_{\text{iso}} = -108$ ppm [33]). They contain 2.0 % of the ^{19}F nuclei of which slightly more than half in CaF_2 . The ^{19}F δ_{iso} values of the NMR resonances assigned to $\text{CaTiF}_6(\text{H}_2\text{O})_2$ range from 45.5 to 105.0 ppm and are then representative of non-bridging (two $\text{TiF}_{6-y}\text{X}_y$ octahedra) F atoms in fluorotitanates [6,53–59] or terminal F atoms in hydroxyfluorinated anatase [43] (**Table 6**). $\text{CaTiF}_6(\text{H}_2\text{O})_2$ presents a fairly wide range of ^{19}F δ_{iso} values which may seem surprising at first sight since five out of the six F atoms, those bridging TiF_6 octahedra and $[\text{CaF}_5(\text{H}_2\text{O})_3]$ SAP, have similar environments with respect to titanium and calcium (**Table S2**). It can be explained by the high sensitivity of the ^{19}F δ_{iso} values to the Ti-F bond length of F atoms bonded to a single Ti atom, as shown on **Fig. 8**, and as observed for the terminal F atoms of TiF_4 whose ^{19}F δ_{iso} values are spread over 57 ppm while the F-Ti bond lengths differ at most by 0.016 Å [60]. In both cases, as expected, the ^{19}F δ_{iso} values increases when the Ti-F bond length decreases.

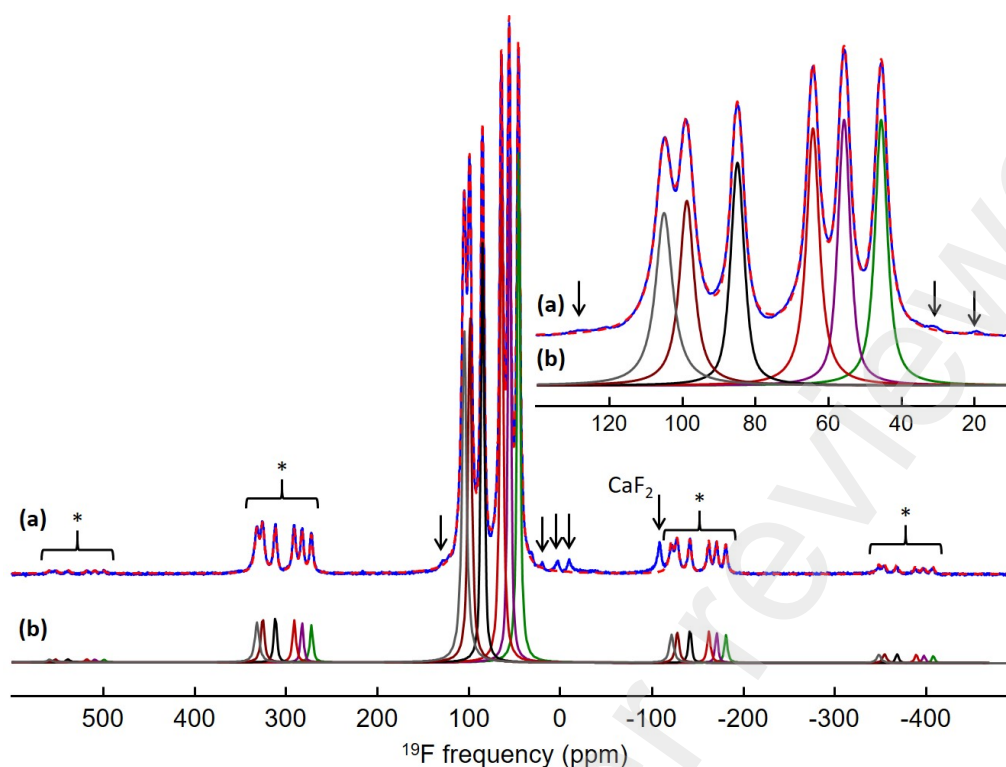


Fig. 7. (a) Experimental (blue line) and fitted (dashed red line) ^{19}F MAS (64 kHz) NMR spectra of $\text{CaTiF}_6(\text{H}_2\text{O})_2$, (b) individual resonances used for the fit (see **Table 5**). Inset: zoom on the isotropic lines. Arrows and stars indicate unidentified and CaF_2 impurities and spinning side bands, respectively.

Table 5. ^{19}F isotropic chemical shifts, δ_{iso} (ppm), chemical shift anisotropy, δ_{csa} (ppm), asymmetry parameter of the CSA tensor, η_{csa} , full width at half-maximum, fwhm (ppm), and relative intensities, I (%), of the NMR lines used for the reconstruction of the ^{19}F MAS (64 kHz) NMR spectrum of $\text{CaTiF}_6(\text{H}_2\text{O})_2$ (**Fig. 7**).

| Line | $\delta_{\text{iso}} (\pm 0.5)$ | $\delta_{\text{csa}} (\pm 20)$ | $\eta_{\text{csa}} (\pm 0.2)$ | fwhm (± 0.1) | $I (\pm 1.0)$ |
|------|---------------------------------|--------------------------------|-------------------------------|--------------------|---------------|
| L1 | 45.5 | -217 | 0 | 4.1 | 17.1 |
| L2 | 55.7 | -223 | 0 | 4.0 | 16.2 |
| L3 | 64.2 | -234 | 0 | 4.3 | 18.4 |
| L4 | 84.9 | -253 | 0.18 | 4.4 | 15.2 |
| L5 | 98.8 | -274 | 0.03 | 4.9 | 15.8 |
| L6 | 105.0 | -272 | 0 | 5.6 | 17.3 |

Table 6. ^{19}F isotropic chemical shifts, δ_{iso} (ppm), of non-bridging (two $\text{TiF}_{6-y}\text{X}_y$ octahedra) F atoms in fluorotitanates and terminal F atoms in TiF_4 and hydroxyfluorinated anatase and correlations between experimental δ_{iso} values and calculated σ_{iso} values.

| Compound | δ_{iso} | Correlation | reference |
|---|-----------------------|--|-----------|
| K_2TiF_6 | 71.4 | | [54] |
| $(\text{NH}_4)_{0.16}\text{K}_{1.84}[\text{Ti}_2\text{F}_2(\text{PO}_4)_2(\text{PO}_3\text{OH})]$ | 78.9 | | [55] |
| $[\text{H}_4\text{tren}] \cdot (\text{TiF}_{4.6}(\text{OH})_{1.4})_2 \cdot 2.7\text{H}_2\text{O}$ | 78.2 to 81.6 | | [56] |
| $\alpha\text{-}[\text{H}_3\text{tren}] \cdot (\text{TiF}_{4.7}(\text{OH})_{1.3}) \cdot (\text{F})$ | 78.8 & 78.9 | | |
| $\beta\text{-}[\text{H}_3\text{tren}] \cdot (\text{TiF}_{4.5}(\text{OH})_{1.5}) \cdot (\text{F})$ | 75.8 to 80.6 | | |
| $(\text{C}_2\text{H}_5\text{N}_4)_2\text{TiF}_6$ | 76 | | [57] |
| $[\text{H}_2\text{taz}]_2 \cdot (\text{Ti}_5\text{O}_5\text{F}_{12})$ | 101.9 | $\delta_{\text{iso}} = -0.97 \sigma_{\text{iso}} + 67.5$ | [53] |
| $[\text{H}_2\text{gua}]_2 \cdot (\text{Ti}_5\text{O}_5\text{F}_{12})$ | 92 | | |
| $\text{trans-Zn}_3\text{TiF}_7(\text{H}_2\text{O})_2(\text{taz})_3 \cdot 3\text{H}_2\text{O}$ | 75.2 | $\delta_{\text{iso}} = -0.82 \sigma_{\text{iso}} + 92$ | [58] |
| $\text{trans-Zn}_3\text{TiF}_7(\text{taz})_3$ | 79.1 | | |
| $\text{cis-Zn}_3\text{TiF}_7(\text{H}_2\text{O})_2(\text{taz})_3 \cdot \text{C}_2\text{H}_5\text{OH}$ | 79.9 | | |
| $\text{cis-Zn}_3\text{TiF}_7(\text{taz})_3$ | 44.2 | | |
| $[\text{Cu}(\text{bpy})_2(\text{H}_2\text{O})]_2[\text{TiF}_6]_2 \cdot 3\text{H}_2\text{O}$ | 83.0 & 93.3 | | [6] |
| $\text{K}_{16}[\text{Mo}_3\text{O}_4\text{F}_9]_2[\text{TiF}_6]_3 \cdot 2\text{H}_2\text{O}$ | 69 & 97, 71 & 37 | $\delta_{\text{iso}} = -0.834 \sigma_{\text{iso}} + 68$ | [59] |
| TiF_4 | 422-480 | $\delta_{\text{iso}} = -1.13 \sigma_{\text{iso}} + 63$ | [60] |
| $\text{Ti}_{0.78}\square_{0.22}\text{O}_{1.12}(\text{OH})_{0.48}\text{F}_{0.40}$ | 98 | | [43] |

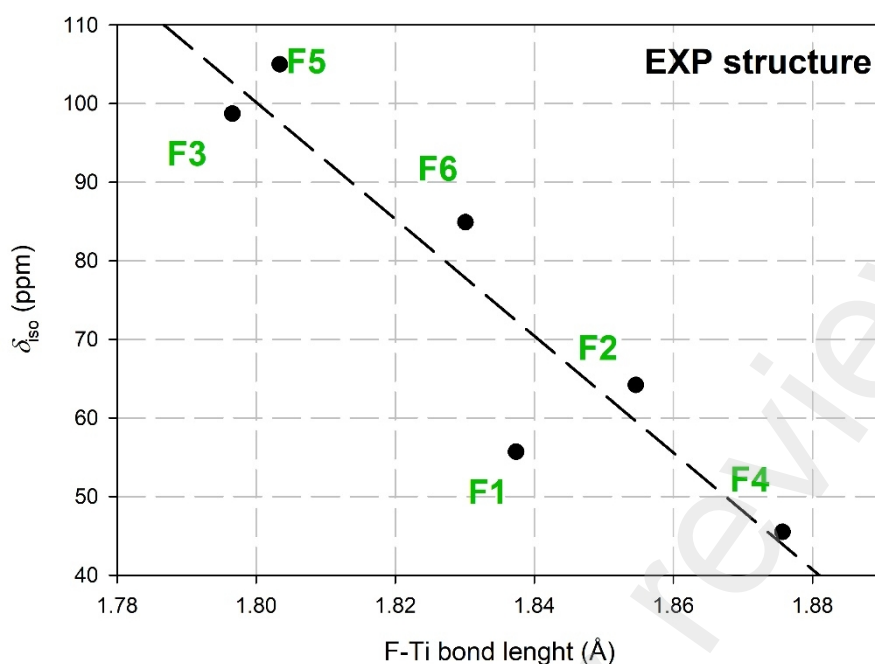


Fig. 8. Experimental ^{19}F δ_{iso} values vs F-Ti bond lengths in $\text{CaTiF}_6(\text{H}_2\text{O})_2$. The dashed black line represents the linear regression.

The absolute values of chemical shift anisotropy (-230 to -270 ppm) are, as expected, in between those of bridging (-147 to -180 ppm) and terminal (-546 to -611 ppm) F atoms in TiF_4 [60].

3.5. NMR modelling parameters

To assign the ^{19}F resonances to the F crystallographic sites, the ^{19}F magnetic shielding tensors have been calculated, using the GIPAW method [17,18] implemented in the NMR-CASTEP code [29,30], for the EXP and APO structures (**Table 7**). NMR lines were ranked in increasing order of experimental δ_{iso} values, F atoms were ranked in decreasing order of calculated σ_{iso} values and these couples of values are plotted in **Fig. 9**. An almost perfect alignment is obtained for the σ_{iso} values computed from the EXP structure. The correlation is significantly poorer with σ_{iso} values calculated from the APO structure. Moreover, EXP and APO structures lead to different NMR line assignments to F sites and the agreement between the experimental and calculated ^{19}F δ_{csa} ($= -\sigma_{csa}$) values (**Table 7**) is better for

the EXP than for the APO structure, for which the σ_{csa} values seem to be overestimated. Similar results were obtained with VASP (**Table S7** and **Fig. S1**). Other optimizations (partial APO using CASTEP, APO and FO optimizations with and without using the semi-empirical DFT-D3 approach [39] using VASP) have been performed without any improvement of the correlation between computed σ_{iso} values and experimental δ_{iso} values (not shown).

Table 7. ^{19}F calculated σ_{iso} (ppm), $\delta_{\text{iso,cal}}$ (ppm), σ_{csa} (ppm) and η_{csa} values of the F sites in the EXP and APO structures of $\text{CaTiF}_6 \cdot 2\text{H}_2\text{O}$, using CASTEP, and experimental $\delta_{\text{iso,exp}}$ (ppm), $\delta_{\text{csa,exp}}$ (ppm) and $\eta_{\text{csa,exp}}$ values of the NMR lines of $\text{CaTiF}_6(\text{H}_2\text{O})_2$. The F sites are assigned to the NMR lines by ranking the F sites in decreasing order of their ^{19}F calculated σ_{iso} values and the NMR lines in increasing order of their experimental δ_{iso} values. The ^{19}F $\delta_{\text{iso,cal}}$ have been calculated by applying the equations of the linear regressions between the calculated σ_{iso} values of the F sites in the EXP and APO structures and the $\delta_{\text{iso,exp}}$ values, *i. e.*, $\delta_{\text{iso,cal}} = -0.612 \sigma_{\text{iso}} + 100.6$ and $\delta_{\text{iso,cal}} = -0.974 \sigma_{\text{iso}} + 88.4$ (**Fig. 9**), respectively.

| F site | Structure | σ_{iso} | $\delta_{\text{iso,exp}}$ | $\delta_{\text{iso,cal}}$ | σ_{csa} | $\delta_{\text{csa,exp}}$ | η_{csa} | $\eta_{\text{csa,exp}}$ |
|---------------|------------------|-----------------------|---------------------------|---------------------------|-----------------------|---------------------------|---------------------|-------------------------|
| F4 | EXP | 86.4 | 45.5 (L1) | 47.7 | 209 | -217 | 0.14 | 0 |
| | APO | 15.0 | 84.9 (L4) | 73.7 | 279 | -253 | 0.25 | 0.18 |
| F1 | EXP | 74.1 | 55.7 (L2) | 55.2 | 233 | -223 | 0.05 | 0 |
| | APO | 37.6 | 45.5 (L1) | 51.8 | 258 | -217 | 0.04 | 0 |
| F2 | EXP | 62.5 | 64.2 (L3) | 62.3 | 232 | -234 | 0.15 | 0 |
| | APO | 27.7 | | 61.4 | 261 | | 0.12 | |
| F6 | EXP | 26.6 | 84.9 (L4) | 84.3 | 277 | -253 | 0.09 | 0.18 |
| | APO | -7.2 | 98.7 (L5) | 95.4 | 313 | -274 | 0.06 | 0.03 |
| F3 | EXP | 4.4 | 98.7 (L5) | 97.9 | 304 | -274 | 0.08 | 0.03 |
| | APO | -23.6 | 105.0 (L6) | 111.3 | 333 | -272 | 0.09 | 0 |
| F5 | EXP | -9.8 | 105.0 (L6) | 106.6 | 294 | -272 | 0.19 | 0 |
| | APO | 28.7 | 55.7 (L2) | 60.4 | 258 | -223 | 0.05 | 0 |

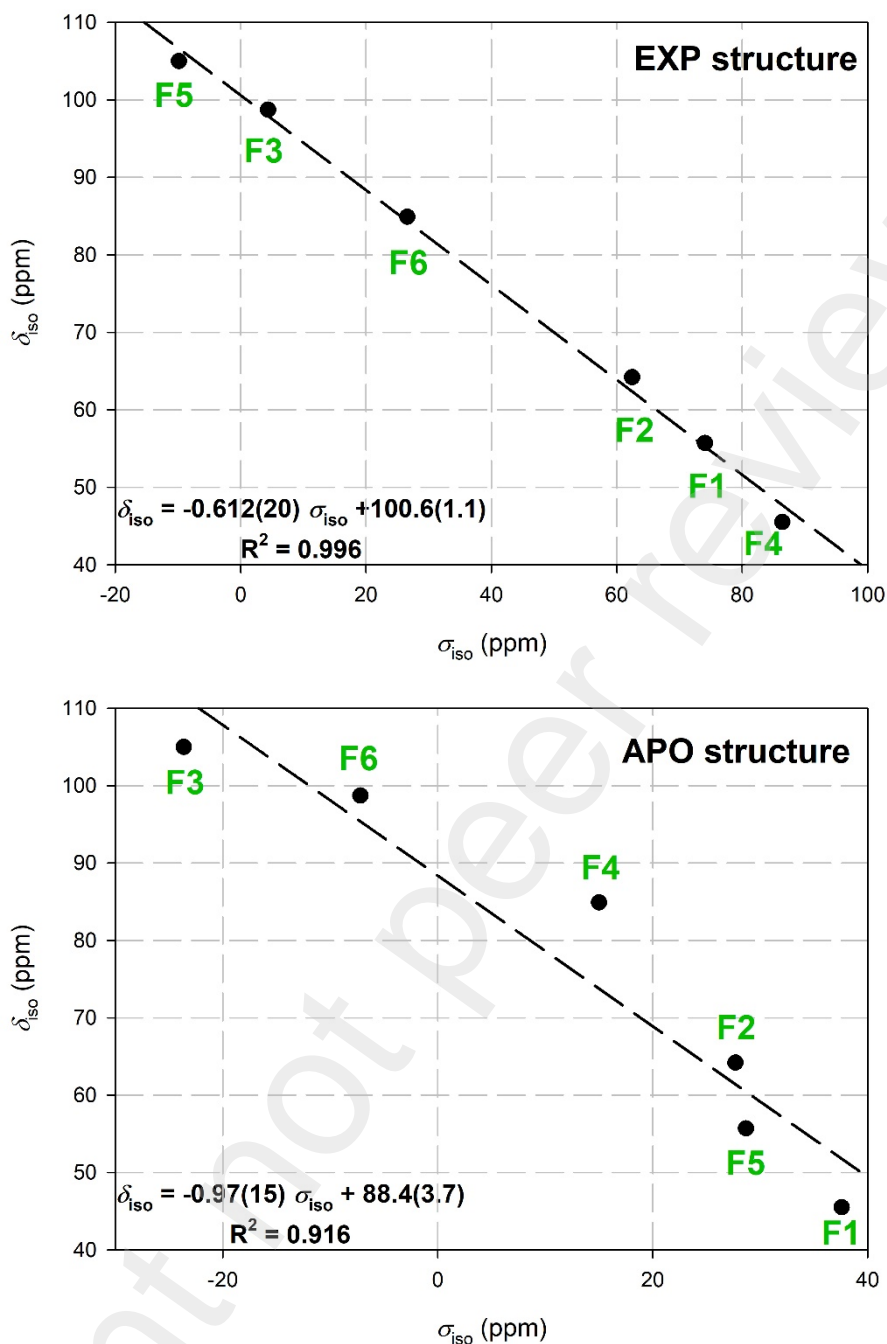


Fig. 9. Experimental ^{19}F δ_{iso} values, ranked in increasing order, versus calculated ^{19}F σ_{iso} values, using CASTEP, ranked in decreasing order, for the EXP (at the top) and the APO (at the bottom) structures of $\text{CaTiF}_6(\text{H}_2\text{O})_2$. The dashed black lines represent the linear regressions whose equations are given.

The optimization of the structure leads to a strengthening of some H-bonds (O2-H3...O1, O1-H2...F5,...) at the detriment of others (**Table 3**), to non-negligible atomic

displacements (Ca: 0.08 Å; O1: 0.18 Å; F5: 0.13 Å; **Table S1**), and consequently to significant environment changes for some F atoms (**Table 8**). Thus, it is clear that DFT optimizations of this structure involving water molecules and H-bonds do not lead to a reliable structural model. This discrepancy between calculated after optimization and experimental data is related to the dynamics of the structural water molecules (rotation, as well as vibration of the H₂O groups) under experimental conditions (at, or close to room temperature) that are not captured by the DFT optimized structure at 0 K. To address this, it is necessary to take into account thermal motions of atomic nuclei, through, for instance, snapshots of ab-initio molecular dynamic simulations [61] at 300 K. This is outside the scope of this study but would be worth testing in the future.

Table 8. Interatomic distances (Å) between F atoms and their first neighbors in the EXP and CASTEP APO structures of CaTiF₆(H₂O)₂ CaTiF₆·2H₂O.

| | | EXP | APO | | | EXP | APO |
|-----------|----|-------|-------|-----------|----|-------|-------|
| F1 | Ti | 1.837 | 1.898 | F2 | Ti | 1.854 | 1.897 |
| | Ca | 2.341 | 2.346 | | Ca | 2.326 | 2.325 |
| | H1 | 2.567 | 2.485 | | | | |
| F3 | Ti | 1.797 | 1.861 | F6 | Ti | 1.830 | 1.861 |
| | Ca | 2.436 | 2.426 | | Ca | 2.331 | 2.329 |
| F4 | Ti | 1.876 | 1.878 | F5 | Ti | 1.803 | 1.899 |
| | H3 | 2.170 | | | H2 | 1.896 | 1.685 |
| | Ca | 2.336 | 2.319 | | H4 | 2.006 | 1.893 |
| | H3 | 2.539 | 2.463 | | H1 | 2.495 | 2.550 |

Finally, the average chemical shift of ¹H calculated from the EXP structure is also in better agreement with the experimental data (**Table 9**). The reconstruction of the ¹H MAS NMR spectrum of CaTiF₆(H₂O)₂, consisting of a main broad line at about 4.6 ppm (**Fig. S2**, **Table S8**), allows determining the ¹H weighted average isotropic chemical shift (4.66 ppm) of the NMR line assigned to H₂O groups. Due to the over-strengthening of the H-

bonds involving H2 and H3, the weighted average calculated ^1H δ_{iso} value is larger for the APO structure than for the EXP one and higher than the average experimental value.

Table 9. ^1H calculated σ_{iso} (ppm) values using CASTEP, $\delta_{\text{iso,cal}}$ (ppm) values of the H sites in the EXP and APO structures of $\text{CaTiF}_6(\text{H}_2\text{O})_2$ and average value of the ^1H $\delta_{\text{iso,cal}}$ values for each structure. The ^1H $\delta_{\text{iso,cal}}$ values have been calculated by applying the equation : $\delta_{\text{iso,cal}} = -\sigma_{\text{iso}} + \sigma_{\text{ref}}$ with $\sigma_{\text{ref}} = 31.0$ ppm [40].

| Structure | EXP | | APO | |
|---|-----------------------|---------------------------|-----------------------|---------------------------|
| | σ_{iso} | $\delta_{\text{iso,cal}}$ | σ_{iso} | $\delta_{\text{iso,cal}}$ |
| H1 | 27.65 | 3.35 | 28.27 | 2.73 |
| H2 | 26.32 | 4.68 | 24.41 | 6.59 |
| H3 | 26.46 | 4.54 | 24.01 | 6.99 |
| H4 | 26.15 | 4.85 | 26.10 | 4.90 |
| <$\delta_{\text{iso,cal}}$> | | 4.36 | | 5.30 |

We then retain the assignment of the F sites to the ^{19}F NMR lines deduced from the EXP structure. The almost perfect alignment obtained for the plot of the computed ^{19}F σ_{iso} values as a function of the experimental δ_{iso} values (**Fig. 9**) demonstrates the accuracy of the EXP structure and provides a reliable assignment. The absolute value of the slope of the linear regression is significantly lower than 1, the theoretical value, and also lower than the other absolute values of slopes previously determined for titanium fluorides (**Table 6**). On the other hand, with the APO structure, the absolute value of the slope is close to 1 (**Fig. 9**). The smaller absolute value of the slope for the EXP structure compared with the APO structure results from the larger range of ^{19}F σ_{iso} values related to shorter and more scattered values of F-Ti bond lengths. The optimization has the well-known effect of minimizing the radial and angular distortions within the polyhedra and the GGA with the PBE overestimates the bond lengths. A smaller range of ^{19}F σ_{iso} values and consequently a larger absolute value of the slope is then obtained for the APO structure.

Although the F-Ti bond lengths are therefore likely to be a little too scattered in the EXP structure, the latter seems to better describe the crystal structure of $\text{CaTiF}_6(\text{H}_2\text{O})_2$.

4. Conclusions

$\text{CaTiF}_6(\text{H}_2\text{O})_2$ adopts the same crystal structure that $\text{SrTiF}_6(\text{H}_2\text{O})_2$. It crystallizes in the monoclinic space group $P2/n$ with cell lengths $a = 5.87976(14) \text{ \AA}$, $b = 10.8546(3) \text{ \AA}$, $c = 9.5096(3) \text{ \AA}$ and $\gamma = 98.9869(8)^\circ$. Its structure is built from the connectivity of dimers $[\text{Ca}_2\text{F}_{10}(\text{H}_2\text{O})_4]$ of distorted SAP $[\text{CaF}_5(\text{H}_2\text{O})_3]$ and TiF_6 octahedra. Each SAP is connected to five different TiF_6 octahedra by F1-4 and F6 atoms. The remaining F5 atom is strongly H-bonded to a proton of the water molecule which not connects two SAP.

The ^{19}F NMR spectrum of $\text{CaTiF}_6(\text{H}_2\text{O})_2$ supports the structural model containing six F sites of same multiplicity. To assign the ^{19}F NMR resonances to the F crystallographic sites, the ^{19}F magnetic shielding tensors have been calculated, using the GIPAW method. The plot of the experimental ^{19}F δ_{iso} values (ranked in increasing order), as a function of the calculated ^{19}F σ_{iso} values (ranked in decreasing order), shows an almost perfect alignment for the EXP structure, demonstrating its accuracy and providing a reliable assignment of the ^{19}F resonances to the F sites. Whereas the dynamics of the structural water molecules under experimental conditions are not captured by the DFT APO structure, leading to a poorer quality of the calculations, the EXP structure provides a good account of the experimental data. The EXP structure better reflects in average the atomic positions.

The BV parameters for the $\text{Ti}^{4+}/\text{F}^-$ ion pair ($R_{ij} = 1.760 \text{ \AA}$ and $b = 0.37 \text{ \AA}$) almost systematically lead to overestimated BVS values for Ti, $\text{CaTiF}_6(\text{H}_2\text{O})_2$ being not one of the exceptions. The value of R_{ij} has been refined with the constraint that the average Ti BVS is equal to its oxidation state, i.e., 4.00 (b remaining equal to its "universal" value) thanks to experimental Ti-F bond lengths from 70 carefully selected structures containing 134 Ti sites forming TiF_6 octahedra. This condition is fulfilled for a value of R_{ij} equal to 1.706 \AA

for which the BVS values range from 3.50 to 4.38 whereas before refinement they ranged from 4.05 to 5.07 and were, in average, equal to 4.63.

Acknowledgements

The CASTEP computations presented in this work have been carried out at the Centre Régional de Calcul Intensif des Pays de la Loire (CCIPL), financed by the French Ministère de la Recherche, the Région Pays de la Loire, and Université de Nantes. The authors thank CCIPL for financial support for CASTEP licenses. This work was granted access to the HPC resources of TGCC (VASP calculations) under the allocation DARI-A0070906303 (2019) attributed by GENCI (Grand Equipement National de Calcul Intensif).

References

- [1] R.L. Davidovich, D.V. Marinin, V. Stavila, K.H. Whitmire, Structural chemistry of fluoride and oxofluoride complexes of titanium(IV), *Coord. Chem. Rev.* 299 (2015) 61–82. <https://doi.org/10.1016/j.ccr.2015.04.002>.
- [2] P. Nugent, V. Rhodus, T. Pham, B. Tudor, K. Forrest, L. Wojtas, B. Space, M. Zaworotko, Enhancement of CO₂ selectivity in a pillared pcu MOM platform through pillar substitution, *Chem. Commun.* 49 (2013) 1606. <https://doi.org/10.1039/c3cc37695h>.
- [3] B.R. Hester, A.P. Wilkinson, Negative Thermal Expansion, Response to Pressure and Phase Transitions in CaTiF₆, *Inorg. Chem.* 57 (2018) 11275–11281. <https://doi.org/10.1021/acs.inorgchem.8b01912>.
- [4] L. Lv, Z. Chen, G. Liu, S. Huang, Y. Pan, Optimized photoluminescence of red phosphor K₂TiF₆:Mn⁴⁺ synthesized at room temperature and its formation mechanism, *J. Mater. Chem. C* 3 (2015) 1935–1941. <https://doi.org/10.1039/C4TC02097A>.
- [5] Q. Zhou, Y. Zhou, Y. Liu, Z. Wang, G. Chen, J. Peng, J. Yan, M. Wu, A new and efficient red phosphor for solid-state lighting: Cs₂TiF₆: Mn⁴⁺, *J. Mater. Chem. C* 3 (2015) 9615–9619. <https://doi.org/10.1039/C5TC02290H>.
- [6] M.L. Nisbet, I.M. Pendleton, G.M. Nolis, K.J. Griffith, J. Schrier, J. Cabana, A.J. Norquist, K.R. Poeppelmeier, Machine-Learning-Assisted Synthesis of Polar Racemates, *J. Am. Chem. Soc.* 142 (2020) 7555–7566. <https://doi.org/10.1021/jacs.0c01239>.
- [7] B.V. Bukvetskii, R.L. Davidovich, V.I. Simonov, The crystal structure of strontium hexafluorotitanate dihydrate, *Koord. Khimiya.* (1975) 1558–1561.
- [8] B.V. Bukvetskii, L.A. Muradyan, M.A. Simonov, V.I. Simonov, Refinement of the crystal structure of strontium hexafluorotitanate dihydrate SrTiF₆(H₂O)₂, *Kristallografiya.* (1979) 29–37.
- [9] T. Chattopadhyay, F. Devreux, K. Peters, E.-M. Peters, E. Gmelin, B. Ghosh, Crystal structure and phase transitions in MnTiF₆·6H₂O and ZnTiF₆·6H₂O, *J. Phys. C Solid State Phys.* 21 (1988) 1321–1334. <https://doi.org/10.1088/0022-3719/21/8/009>.
- [10] G. Mostafa, S. Ray, A. Mukhopadhyay, eds., Studies on some MG₆ · LR₆ compounds. II. Crystal structure of zinc fluotitanate hexahydrate and its low temperature phase, *Z. Für Krist. - Cryst. Mater.* 211 (1996) 373–377. <https://doi.org/10.1524/zkri.1996.211.6.373>.
- [11] P. Halasyamani, M.J. Willis, C.L. Stern, K.R. Poeppelmeier, Crystal growth in aqueous hydrofluoric acid and (HF)_x·pyridine solutions: syntheses and crystal structures of [Ni(H₂O)₆]²⁺[MF₆]²⁻ (M = Ti, Zr, Hf) and Ni₃(py)₁₂F₆·7H₂O, *Inorganica Chim. Acta.* 240 (1995) 109–115. [https://doi.org/10.1016/0020-1693\(95\)04650-X](https://doi.org/10.1016/0020-1693(95)04650-X).
- [12] J. Fischer, G. Keib, R. Weiss, Structure cristalline du fluorotitanate de cuivre tetrahydraté, CuTiF₆·4H₂O, *Acta Crystallogr.* 22 (1967) 338–340. <https://doi.org/10.1107/S0365110X67000659>.
- [13] E.A. Marseglia, I.D. Brown, Lithium hexafluorotitanate dihydrate and lithium hexafluorostannate dihydrate, *Acta Crystallogr. B.* 29 (1973) 1352–1354. <https://doi.org/10.1107/S0567740873004498>.
- [14] I. Ban, M. Kristl, B. Volavšek, L. Golič, Kristallstruktur und thermische Analyse von Hydroxylammonium-hexafluorotitanat(IV)-dihydrat und Hydroxylammonium-hexafluorindat(III), *Monatshefte Für Chem. Chem. Mon.* 130 (1999) 401–408. <https://doi.org/10.1007/PL00010221>.

- [15] D. Mootz, E.-J. Oellers, M. Wiebcke, Hexafluorotitan(IV)-Säure: Untersuchungen zur Bildung und Struktur kristalliner Hydrate, *Z. Für Anorg. Allg. Chem.* 564 (1988) 17–25. <https://doi.org/10.1002/zaac.19885640103>.
- [16] A. Decian, J. Fischer, R. Weiss, Structure cristalline de l'heptafluorotitanate de cuivre et d'ammonium tétrahydraté, $\text{NH}_4\text{CuTiF}_7 \cdot 4\text{H}_2\text{O}$, *Acta Crystallogr.* 22 (1967) 340–343. <https://doi.org/10.1107/S0365110X67000660>.
- [17] C.J. Pickard, F. Mauri, All-electron magnetic response with pseudopotentials: NMR chemical shifts, *Phys. Rev. B.* 63 (2001) 245101. <https://doi.org/10.1103/PhysRevB.63.245101>.
- [18] J.R. Yates, C.J. Pickard, F. Mauri, Calculation of NMR chemical shifts for extended systems using ultrasoft pseudopotentials, *Phys. Rev. B.* 76 (2007) 024401. <https://doi.org/10.1103/PhysRevB.76.024401>.
- [19] H.M. Rietveld, A profile refinement method for nuclear and magnetic structures, *J. Appl. Crystallogr.* 2 (1969) 65–71. <https://doi.org/10.1107/S0021889869006558>.
- [20] J. Rodriguez-Carvajal, Magnetic Structure Determination from Powder Diffraction using the Program *FullProf*, in: *Appl. Crystallogr.*, WORLD SCIENTIFIC, Wisla, Poland, 2001: pp. 30–36. https://doi.org/10.1142/9789812811325_0005.
- [21] C.R. Groom, I.J. Bruno, M.P. Lightfoot, S.C. Ward, The Cambridge Structural Database, *Acta Crystallogr. Sect. B Struct. Sci. Cryst. Eng. Mater.* 72 (2016) 171–179. <https://doi.org/10.1107/S2052520616003954>.
- [22] D. Massiot, F. Fayon, M. Capron, I. King, S. Le Calvé, B. Alonso, J.-O. Durand, B. Bujoli, Z. Gan, G. Hoatson, Modelling one- and two-dimensional solid-state NMR spectra, *Magn. Reson. Chem.* 40 (2002) 70–76. <https://doi.org/10.1002/mrc.984>.
- [23] S. Kang, K.G. Reeves, I. Aguilar, A.G. Porras Gutierrez, J.-C. Badot, S. Durand-Vidal, C. Legein, M. Body, A. Iadecola, O.J. Borkiewicz, O. Dubrunfaut, F. Fayon, P. Florian, D. Dambournet, Ordering of a Nanoconfined Water Network around Zinc Ions Induces High Proton Conductivity in Layered Titanate, *Chem. Mater.* 34 (2022) 3967–3975. <https://doi.org/10.1021/acs.chemmater.1c04421>.
- [24] I.D. Brown, D. Altermatt, Bond-valence parameters obtained from a systematic analysis of the Inorganic Crystal Structure Database, *Acta Crystallogr. B.* 41 (1985) 244–247. <https://doi.org/10.1107/S0108768185002063>.
- [25] N.E. Brese, M. O'Keeffe, Bond-valence parameters for solids, *Acta Crystallogr. B.* 47 (1991) 192–197. <https://doi.org/10.1107/S0108768190011041>.
- [26] H. Zheng, K.M. Langner, G.P. Shields, J. Hou, M. Kowiel, F.H. Allen, G. Murshudov, W. Minor, Data mining of iron(II) and iron(III) bond-valence parameters, and their relevance for macromolecular crystallography, *Acta Crystallogr. Sect. Struct. Biol.* 73 (2017) 316–325. <https://doi.org/10.1107/S2059798317000584>.
- [27] S. Adams, Global instability index optimizations for the localization of mobile protons, *Solid State Ion.* 168 (2004) 281–290. <https://doi.org/10.1016/j.ssi.2003.04.002>.
- [28] I.D. Brown, *The Chemical Bond in Inorganic Chemistry*, Oxford University Press, 2016. <https://doi.org/10.1093/acprof:oso/9780198742951.001.0001>.
- [29] M.D. Segall, P.J.D. Lindan, M.J. Probert, C.J. Pickard, P.J. Hasnip, S.J. Clark, M.C. Payne, First-principles simulation: ideas, illustrations and the CASTEP code, *J. Phys. Condens. Matter.* 14 (2002) 2717–2744. <https://doi.org/10.1088/0953-8984/14/11/301>.
- [30] S.J. Clark, M.D. Segall, C.J. Pickard, P.J. Hasnip, M.I.J. Probert, K. Refson, M.C. Payne, First principles methods using CASTEP, *Z. Für Krist. - Cryst. Mater.* 220 (2005) 567–570. <https://doi.org/10.1524/zkri.220.5.567.65075>.

- [31] J.P. Perdew, K. Burke, M. Ernzerhof, Generalized Gradient Approximation Made Simple, *Phys. Rev. Lett.* 77 (1996) 3865–3868. <https://doi.org/10.1103/PhysRevLett.77.3865>.
- [32] M. Profeta, F. Mauri, C.J. Pickard, Accurate First Principles Prediction of ^{17}O NMR Parameters in SiO_2 : Assignment of the Zeolite Ferrierite Spectrum, *J. Am. Chem. Soc.* 125 (2003) 541–548. <https://doi.org/10.1021/ja027124r>.
- [33] A. Sadoc, M. Body, C. Legein, M. Biswal, F. Fayon, X. Rocquefelte, F. Boucher, NMR parameters in alkali, alkaline earth and rare earth fluorides from first principle calculations, *Phys. Chem. Chem. Phys.* 13 (2011) 18539. <https://doi.org/10.1039/c1cp21253b>.
- [34] B.G. Pfrommer, M. Côté, S.G. Louie, M.L. Cohen, Relaxation of Crystals with the Quasi-Newton Method, *J. Comput. Phys.* 131 (1997) 233–240. <https://doi.org/10.1006/jcph.1996.5612>.
- [35] G. Kresse, J. Furthmüller, Efficient iterative schemes for *ab initio* total-energy calculations using a plane-wave basis set, *Phys. Rev. B.* 54 (1996) 11169–11186. <https://doi.org/10.1103/PhysRevB.54.11169>.
- [36] G. Kresse, J. Furthmüller, Efficiency of *ab-initio* total energy calculations for metals and semiconductors using a plane-wave basis set, *Comput. Mater. Sci.* 6 (1996) 15–50. [https://doi.org/10.1016/0927-0256\(96\)00008-0](https://doi.org/10.1016/0927-0256(96)00008-0).
- [37] G. Kresse, D. Joubert, From ultrasoft pseudopotentials to the projector augmented-wave method, *Phys. Rev. B.* 59 (1999) 1758–1775. <https://doi.org/10.1103/PhysRevB.59.1758>.
- [38] P.E. Blöchl, Projector augmented-wave method, *Phys. Rev. B.* 50 (1994) 17953–17979. <https://doi.org/10.1103/PhysRevB.50.17953>.
- [39] S. Grimme, J. Antony, S. Ehrlich, H. Krieg, A consistent and accurate *ab initio* parametrization of density functional dispersion correction (DFT-D) for the 94 elements H-Pu, *J. Chem. Phys.* 132 (2010) 154104. <https://doi.org/10.1063/1.3382344>.
- [40] C. Gervais, M. Profeta, V. Lafond, C. Bonhomme, T. Azaïs, H. Mutin, C.J. Pickard, F. Mauri, F. Babonneau, Combined *ab initio* computational and experimental multinuclear solid-state magnetic resonance study of phenylphosphonic acid, *Magn. Reson. Chem.* 42 (2004) 445–452. <https://doi.org/10.1002/mrc.1360>.
- [41] B.T.M. Willis, The anomalous behaviour of the neutron reflexion of fluorite, *Acta Crystallogr.* 18 (1965) 75–76. <https://doi.org/10.1107/S0365110X65000130>.
- [42] M. Horn, C.F. Schwerdtfeger, E.P. Meagher, Refinement of the structure of anatase at several temperatures, *Z. Für Krist.* 136 (1972) 273–281. <https://doi.org/10.1524/zkri.1972.136.3-4.273>.
- [43] W. Li, D. Corradini, M. Body, C. Legein, M. Salanne, J. Ma, K.W. Chapman, P.J. Chupas, A.-L. Rollet, C. Julien, K. Zhagib, M. Duttine, A. Demourgues, H. Groult, D. Dambournet, High Substitution Rate in TiO_2 Anatase Nanoparticles with Cationic Vacancies for Fast Lithium Storage, *Chem. Mater.* 27 (2015) 5014–5019. <https://doi.org/10.1021/acs.chemmater.5b01407>.
- [44] J. Ravez, M. Vassiliadis, R. von der Muehll, P. Hagenmuller, Les systèmes $\text{MF}_2\text{-TiF}_4$ (M = Ca, Sr, Ba), *Rev. Chim. Minérale.* (1970) 967–973.
- [45] D. Zagorac, H. Müller, S. Ruehl, J. Zagorac, S. Rehme, Recent developments in the Inorganic Crystal Structure Database: theoretical crystal structure data and related features, *J. Appl. Crystallogr.* 52 (2019) 918–925. <https://doi.org/10.1107/S160057671900997X>.

- [46] M. Feist, E. Kemnitz, Applications of PulseTA® to the investigation of fluorides: An attempt to calibrate HF, *Thermochim. Acta.* 446 (2006) 84–90. <https://doi.org/10.1016/j.tca.2006.04.021>.
- [47] A. Demourgues, N. Penin, E. Durand, F. Weill, D. Dambournet, N. Viadere, A. Tressaud, New Titanium Hydroxyfluoride $\text{Ti}_{0.75}(\text{OH})_{1.5}\text{F}_{1.5}$ as a UV Absorber, *Chem. Mater.* 21 (2009) 1275–1283. <https://doi.org/10.1021/cm8030297>.
- [48] V.L. Deringer, V. Hoepfner, R. Dronskowski, Accurate Hydrogen Positions in Organic Crystals: Assessing a Quantum-Chemical Aide, *Cryst. Growth Des.* 12 (2012) 1014–1021. <https://doi.org/10.1021/cg201505n>.
- [49] A. Zeidler, P.S. Salmon, H.E. Fischer, J.C. Neufeind, J. Mike Simonson, T.E. Markland, Isotope effects in water as investigated by neutron diffraction and path integral molecular dynamics, *J. Phys. Condens. Matter.* 24 (2012) 284126. <https://doi.org/10.1088/0953-8984/24/28/284126>.
- [50] D.L. Kepert, *Inorganic Stereochemistry*, Springer Berlin Heidelberg, Berlin, Heidelberg, 1982. <https://doi.org/10.1007/978-3-642-68046-5>.
- [51] A. Bondi, van der Waals Volumes and Radii, *J. Phys. Chem.* 68 (1964) 441–451. <https://doi.org/10.1021/j100785a001>.
- [52] E. Arunan, G.R. Desiraju, R.A. Klein, J. Sadlej, S. Scheiner, I. Alkorta, D.C. Clary, R.H. Crabtree, J.J. Dannenberg, P. Hobza, H.G. Kjaergaard, A.C. Legon, B. Mennucci, D.J. Nesbitt, Definition of the hydrogen bond (IUPAC Recommendations 2011), *Pure Appl. Chem.* 83 (2011) 1637–1641. <https://doi.org/10.1351/PAC-REC-10-01-02>.
- [53] M. Albino, M. Body, C. Legein, A. Hémon-Ribaud, M. Leblanc, V. Maisonneuve, J. Lhoste, NMR Crystallography, Hydrogen Bonding and Optical Properties of the Novel 2D Hybrid Oxyfluorotitanate $[\text{H}_2\text{taz}]_2 \cdot (\text{Ti}_5\text{O}_5\text{F}_{12})$, *Cryst. Growth Des.* 18 (2018) 6873–6884. <https://doi.org/10.1021/acs.cgd.8b01085>.
- [54] C.J.L. Silwood, I. Abrahams, D.C. Apperley, N.P. Lockyer, E. Lynch, M. Motevalli, R.M. Nix, M. Grootveld, Surface analysis of novel hydroxyapatite bioceramics containing titanium(IV) and fluoride, *J. Mater. Chem.* 15 (2005) 1626–1636. <https://doi.org/10.1039/B417539E>.
- [55] S. Yang, G. Li, W. Liu, W. Wang, Z. Yan, Y. Huang, F. Liao, J. Lin, Synthesis and Characterization of a Fluorotitanophosphate $(\text{NH}_4)_{0.16}\text{K}_{1.84}[\text{Ti}_2\text{F}_2(\text{PO}_4)_2(\text{PO}_3\text{OH})]$ with a Unique Lamella Framework, *Inorg. Chem.* 48 (2009) 5449–5453. <https://doi.org/10.1021/ic900504m>.
- [56] J. Lhoste, M. Body, C. Legein, A. Ribaud, M. Leblanc, V. Maisonneuve, F⁻/OH⁻ substitution in $[\text{H}_4\text{tren}]^{4+}$ and $[\text{H}_3\text{tren}]^{3+}$ hydroxyfluorotitanates(IV) and classification of tren cation configurations, *J. Solid State Chem.* 217 (2014) 72–79. <https://doi.org/10.1016/j.jssc.2014.05.008>.
- [57] V.Ya. Kavun, R.L. Davidovich, V.B. Logvinova, E.B. Merkulov, V.V. Tkachev, Synthesis, crystal structure, and NMR investigation of 4-amino-1,2,4-triazolium hexafluoridotitanate(IV), *J. Fluor. Chem.* 178 (2015) 68–72. <https://doi.org/10.1016/j.jfluchem.2015.06.027>.
- [58] M. Albino, J. Lhoste, M. Body, C. Legein, A. Hémon-Ribaud, V. Maisonneuve, M. Leblanc, Topotactic desolvation and condensation reactions of 3D $\text{Zn}_3\text{TiF}_7(\text{H}_2\text{O})_2(\text{taz})_3 \cdot \text{S}$ (S = 3H₂O or C₂H₅OH), *Dalton Trans.* 49 (2020) 17758–17771. <https://doi.org/10.1039/D0DT03391J>.
- [59] F. Ding, K.J. Griffith, C.P. Koçer, R.J. Saballos, Y. Wang, C. Zhang, M.L. Nisbet, A.J. Morris, J.M. Rondinelli, K.R. Poeppelmeier, Multimodal Structure Solution with ¹⁹F NMR Crystallography of Spin Singlet Molybdenum Oxyfluorides, *J. Am. Chem. Soc.* 142 (2020) 12288–12298. <https://doi.org/10.1021/jacs.0c04019>.

- [60] M. Murakami, Y. Noda, K. Takegoshi, Terminal and bridging fluorine ligands in TiF_4 as studied by ^{19}F NMR in solids, *Solid State Nucl. Magn. Reson.* 101 (2019) 82–88. <https://doi.org/10.1016/j.ssnmr.2019.05.007>.
- [61] J.-N. Dumez, C.J. Pickard, Calculation of NMR chemical shifts in organic solids: Accounting for motional effects, *J. Chem. Phys.* 130 (2009) 104701. <https://doi.org/10.1063/1.3081630>.